Journal of Magnetism and Magnetic Materials 469 (2019) 550–557

Contents lists available at ScienceDirect

Journal of Magnetism and Magnetic Materials

journal homepage: www.elsevier.com/locate/jmmm

Research articles

Nano-sized ferrite particles for magnetic resonance imaging thermometry

J.H. Hankiewicz[a,*], J.A. Stoll[b], J. Stroud[a], J. Davidson[a], K.L. Livesey[a], K. Tvrdy[b], A. Roshko[c,1], S.E. Russek[c], K. Stupic[c], P. Bilski[d], R.E. Camley[a], Z.J. Celinski[a]

[a] University of Colorado, Colorado Springs Center for the Biofrontiers Institute, 1420 Austin Bluffs Pkway, CO 80918, USA
[b] University of Colorado, Colorado Springs, Department of Chemistry & Biochemistry, 1420 Austin Bluffs Pkway, CO 80918, USA
[c] National Institute of Standards and Technology, 325 Broadway St., Boulder, CO 80305, USA
[d] Department of Physics, A. Mickiewicz University, Ul. Umultowska 85, 61-614 Poznan, Poland

ARTICLE INFO

Keywords:
MRI thermometry
Magnetic nanoparticles
Ferrites
Transverse relaxivity
Longitudinal relaxivity

ABSTRACT

Recently, we reported the application of magnetic particles as temperature sensors for use in magnetic resonance imaging thermometry (tMRI). In this novel method, the brightness of the magnetic resonance (MR) image changes with temperature due to a temperature-dependent local magnetic field inhomogeneity caused by the dipolar field of the magnetic particles. Ferrites are new and promising compounds for tMRI applications because of their biocompatibility and because their magnetic properties can be varied by changing composition. Earlier studies used micrometer sized ferrite particles in a proof-of-concept demonstration. However, such large particles cannot be administered intravenously for *in-vivo* use. In this report, we establish the use of nanoscale ferrite particles as temperature sensors for tMRI. Scanning transmission electron microscopy and X-ray diffraction demonstrate the synthesis of 210 nm $Co_{0.3}Zn_{0.7}Fe_2O_4$ clusters comprised of 10–30 nm crystallites. Temperature-dependent magnetization measurements reveal a Curie temperature of around 275 K. We conducted nuclear magnetic resonance (NMR) and MRI studies of samples with different concentrations of ferrite nanoparticles suspended in agar gel. The relative MR image intensity shows a near-linear temperature dependence. At concentrations as low as 0.12 g/L these ferrite nanoparticles provide sufficient image contrast to determine temperature changes with accuracy of ± 1.0 K at 310 K, bolstering the potential viability of this material for biomedical applications.

1. Introduction

The magnetic resonance imaging thermometry technique (tMRI) promises to be a valuable tool for medical professionals due to its ability to noninvasively create a detailed overlaid map of both temperature and tissue water proton density [1–3]. One promising aspect of tMRI is the potential to utilize traditional, in-place magnetic resonance imaging (MRI) scanners to collect such information, lowering the clinical cost of obtaining spatio-thermal data.

Elevated physiological temperature has long been used as an indicator of disease as fever represents a universal immune response [4]. For example, temperature increases have been used to diagnose both potentially lethal tissue malperfusion following surgery and other maladies such as peripheral neuropathy [5]. Further, a localized increase in temperature of 1.5° has been observed in growing tumors [6,7], suggesting temperature-mapping as a potential diagnostic tool. Accurately monitoring temperature is also necessary for safety purposes in MRI guided thermal ablation procedures (radio-frequency, laser, or focused ultrasound) where there exists a need to deliver high energy to a treated area while simultaneously protecting adjacent healthy tissue [8–10].

Currently, the most common method of determining temperature via MRI is by the phase shift of proton resonance frequency (PRF). This method is based on an approximately −0.01 ppm/°C temperature dependence in water proton chemical shift [11]. However, PRF suffers several drawbacks, such as sensitivity to both physiological movement [12] and unstable magnetic fields [13,14]. In addition, PRF also becomes impractical in the presence of adipose tissue [15–17].

We have previously reported the method of using micrometer size magnetic particles as exogenous MRI temperature contrast agents that can make temperature measurements more robust [18–20]. These particles, suspended in tissue-mimicking agar gel phantoms, exhibit a strong change in magnetization over the physiologically relevant temperature range (290–330 K), and as a result, introduce a temperature-

* Corresponding author.
E-mail address: jhankiew@uccs.edu (J.H. Hankiewicz).
[1] Contribution of the US Government, not subject to copyright.

https://doi.org/10.1016/j.jmmm.2018.09.037
Received 26 June 2018; Received in revised form 1 August 2018; Accepted 7 September 2018
Available online 08 September 2018

dependent inhomogeneity in the local magnetic field. This inhomogeneity can then be measured in T_2^* weighted gradient-echo MR images [21,22]. A decrease of magnetic moment with increasing temperature causes regions with a higher temperature to appear brighter, generating temperature dependent contrast. However, the size of these particles lay outside of the physiologically tolerable range for the proper biodistribution [23,24]. This work demonstrates that magnetic nanoparticles, with their Curie temperature below body temperature, can also be used as MRI temperature contrast agents.

While any magnetic particles with strong thermal dependence of magnetic moment can serve as temperature sensors for MRI thermometry, ferrites represent a uniquely versatile class of magnetic materials due to the strong effects of chemical composition, crystallographic structure, and morphology on their magnetic properties [25–28]. Ferrite nanoparticles have already been employed as MRI contrast agents targeting the liver and spleen [24,29,30] and are also widely studied for other medical applications, such as hyperthermia therapy [30–34]. Cobalt ferrites have garnered attention due to their relatively high saturation magnetization [35,36]. In particular, the composition $Co_{0.3}Zn_{0.7}Fe_2O_4$ was chosen for this study due to an observed steep decline in magnetic moment near body temperature, which permitted accurate temperature measurement based on changes of brightness in T_2^* weighted MR images [37].

In this work, the initial results of employing $Co_{0.3}Zn_{0.7}Fe_2O_4$ ferrite nanoparticles as MRI contrast agents are presented. The nanoparticles were synthesized by hydrolysis of metallic salts in an aqueous solution. Scanning transmission electron microscopy (STEM), scanning electron microscopy (SEM) and X-ray diffraction (XRD) were used to determine size and the structural properties of the synthesized nanoparticles, while a Superconductive Quantum Interference Device (SQUID) magnetometer was used to perform non-spatial magnetic characterization over a wide temperature range. Nuclear Magnetic Resonance (NMR) and MRI systems were used to gather spatio-thermal data relevant to the influence of ferrite nanoparticles within tissue-mimicking phantoms. Collectively, these studies demonstrate that a low nanoparticle concentration produces the contrast in MRI images necessary for temperature determination with resolution higher than ± 1.0 K at 310 K.

2. Material and methods

Nanoparticles with the composition $Co_{0.3}Zn_{0.7}Fe_2O_4$ were synthesized based on a previously reported colloidal method [38,39]. Cobalt chloride hexahydrate ($CoCl_2{\cdot}6H_2O$, 98%), ferric chloride hexahydrate ($FeCl_3{\cdot}6H_2O$, 97%), and anhydrous zinc chloride ($ZnCl_2$, 98%) were dissolved in 18 MΩ deionized water to make an amber-colored solution of 4.95 mM $CoCl_2{\cdot}6H_2O$, 11.6 mM $ZnCl_2$, and 33.0 mM $FeCl_3{\cdot}6H_2O$ with a pH of 2.1. Each synthesis was performed by heating 50 mL of a 0.25 M 1,6-hexanediamine (HMDA, 98%) solution of pH 11.9 to 353 K while stirring at 800 RPM using a magnetic stir bar. A 50 mL volume of the metal ion solution was added to the stirring HDMA solution using a syringe pump set to dispense at a rate of 2 mL/min, immediately precipitating dark-brown particles upon addition. The solution was stirred at 353 K for 4 h at a rate of 800 RPM (ending pH 11.0). Particles were isolated through retention of the pellet following centrifugation at $4800 \times g$ for 10 min. Washing was performed through iterative addition, mixing, and subsequent centrifugation ($4800 \times g$, 10 min) of 20 mL volumes of 0.25 M HMDA solution. To thermally degrade the remaining HMDA, the nanoparticles were dried and annealed at 1070 K under ambient atmosphere for 15 min.

Nanoparticle stoichiometric composition was verified using flame atomic absorption and energy dispersive x-ray spectroscopy (data not shown). X-ray diffraction measurements were carried out using Kα-Cu radiation in parallel beam configuration with a graphite diffraction grating monochromator. The average ferrite cluster size and distribution were determined using scanning electron microscopy. Scanning transmission electron microscopy was used for analysis of sizes of individual crystallites. Samples for STEM imaging were prepared by dispersing the ferrite particles in isopropanol and drop casting onto lacey carbon coated copper grids, which were subsequently dried at 150 °C for 1 h under ambient conditions. Imaging was performed at an electron acceleration of 200 kV.

The magnetic properties of the ferrite nanoparticles were studied using a SQUID magnetometer. Two samples were used for the measurements of the temperature dependence of magnetization; a 1.0 mg sample for measurements in an applied field of 3 T, and an 8.4 mg sample for low-field measurements (2–20 mT). The magnetic moment of the nanoparticles was measured in low fields using both zero field cooling (ZFC) and field cooling (FC) modes in the 4–350 K temperature range.

Measurements of the water proton NMR linewidth and relaxation times T_1 and T_2 were taken in a 3 T magnetic field as a function of temperature. Both reference (2% agar solution in deionized water) and sensitized (the same agar gel with embedded ferrite nanoparticles of 0.12 g/L concentration) phantoms were prepared. The inversion recovery and Carr Purcell Meiboom Gill (CPMG) methods were used to determine the relaxation times T_1 and T_2, respectively [40].

For each MRI temperature measurement, two phantoms (cylindrical tubes 10 mm in diameter and 80 mm long) were imaged; the first containing the reference sample of pure agar gel and the second contained agar gel with embedded ferrite nanoparticles. The bottom half of the second cylinder was filled with agar gel containing particles at concentration 0.24 g/L. After solidifying gel in ice water, the remaining space in the cylinder was filled with the gel having particle concentration of 0.12 g/L. The details of thermal control during MRI imaging are described in our previous paper [20].The gradient echo method (GEM, sensitive to the inhomogeneity of local magnetic fields) [41] was used with: axial slice orientation, 3 cm × 3 cm field of view, 0.47 mm/pixel in-plane resolution, 6 mm slice thickness, 100 ms repetition time (TR), 2.676 ms echo time (TE), and a radio-frequency flip-angle of 20°. Images were acquired in a research MR scanner with a 30 cm bore at an applied static field (B_o) of 3 T.

Particles were checked 12 months after the fabrication for stability. Dry particles were tested using SQUID for mass magnetization changes after storage at room temperature. Aqueous solution of particles in 0.12 g/L concentration was tested after storage at 4 °C by measurement of R_2^* relaxivity using pulse NMR.

3. Results and discussion

3.1. Structural characterization

The formation of a single crystal phase of inverse spinel ferrites was confirmed by XRD analysis, Fig. 1. The measured lattice constant a = 0.8419 nm agrees with values reported in the literature [42]. The observed Full Width at Half Maximum (FWHM) of the XRD peaks (see Fig. 1) allowed the determination of the average crystallite size of 13.2 nm using the Scherrer formula [43]. Ferrite nanoparticle crystallinity and size were further probed with STEM. Fig. 2**a and b** show STEM bright field images of ferrite nanoparticles at different magnifications. The images show agglomerates consisting of crystallites ranging in size from 10 to 30 nm. All the acquired STEM images allowed us to determine the crystallites size distribution, which can be fit with log-normal functions (see Fig. 2**c**). The acquired data indicates a trinomial distribution of crystallite sizes, with average crystallite sizes of 10.4 (± 1.0), 16.5 (± 3.4) and 27.3 (± 2.3) nm, where the number in brackets is the standard deviation for each population. The percentage of particles in each population is 24, 66 and 10, respectively. Such a size distribution will have a detrimental effect on magnetic behavior and clearly indicates that sample preparation needs further improvements to obtain monodisperse nanoparticle distribution. The analysis of STEM images, however, agrees with XRD analysis that predicted crystallite of 13.2 nm average size.

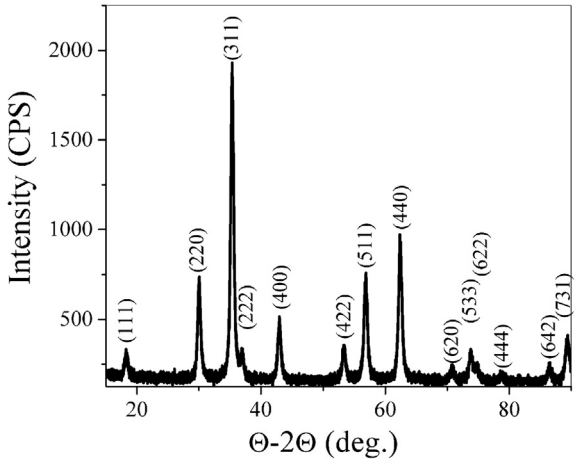

Fig. 1. XRD Θ-2Θ measurements of the annealed $Co_{0.3}Zn_{0.7}Fe_2O_4$ nanoparticles.

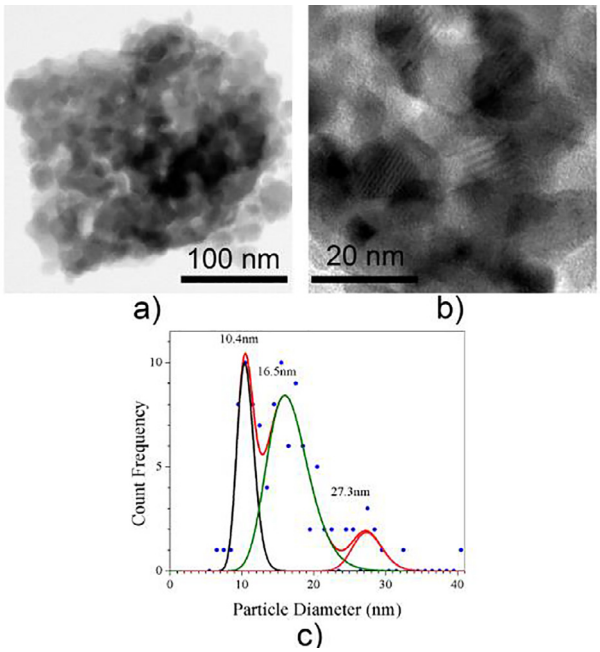

Fig. 2. STEM images of prepared nanoparticles at different magnification (a) 320 × 320 nm; and (b) 97 × 97 nm field of view, respectively. (c) Size distribution based on measured 122 crystallites and curve fit using log-normal functions. The thick red line represents the envelop of the three log-normal curves. (For interpretation of the references to colour in this figure legend, the reader is referred to the web version of this article.)

Fig. 2**a** shows a typical agglomerate of crystallites obtained after annealing at 1070 K. Such agglomerated material was used to carry out the magnetometry, NMR, and MRI studies. Analysis of SEM images determined the average size of agglomerates to be 210 nm with 90 nm standard deviation. We noticed that the sonication can be used to reduce the agglomerate size. After 2 h of sonication with 30 W of power, and two days sedimentation of heavy particles, we carried out dynamic light scattering measurements (DLS) that reveal an average hydrodynamic diameter of 49 nm ± 20 nm. These results indicate that one can reduce the size of agglomerates to a few individual nanoparticles. Eventually, one could prevent re-agglomeration of individual nanoparticles in aqueous solutions by using surfactant coating. The deliberate use of agglomerates (100 nm comprised of 5–15 nm crystallites) by others has demonstrated high magnetic field inhomogeneity for more efficient R_2^* transverse relaxivity [44].

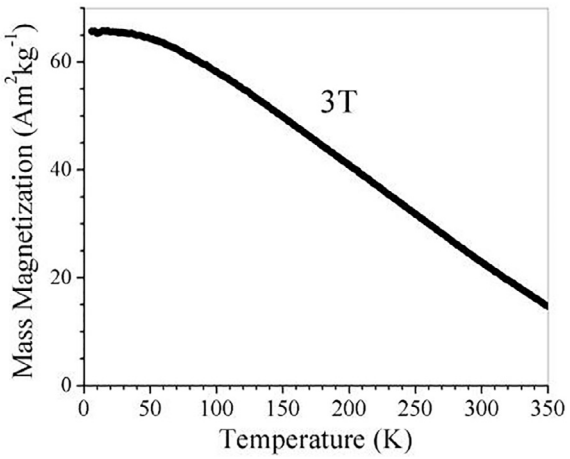

Fig. 3. The temperature dependence of mass magnetization at 3 T applied field.

3.2. Magnetization measurements

The mass magnetization (3 T field) of synthesized particles as a function of temperature is shown in Fig. 3. The value of the mass magnetization measured at 5 K (65.7 Am^2kg^{-1}) is in agreement with values reported for particles of similar size, [45,46] but is smaller than that of bulk material [47]. A strong linear dependence of magnetization upon temperature was observed with the highest applied field of 3 T for temperatures above 80 K (Fig. 3). In the range of 278 K to 334 K, the slope was $-0.169\ Am^2\,kg^{-1}K^{-1}$, similar to that of $-0.245\ Am^2kg^{-1}K^{-1}$ reported for 5 μm Gd particles in our previous proof-of-concept paper [18]. This strong temperature dependence suggests that these ferrite nanoparticles can be employed as MRI temperature contrast agents.

Hysteresis loops of ferrite nanoparticles at several temperatures ranging from 4 K to 310 K are shown in Fig. 4. At low temperatures (4 K and 8 K) a typical behavior for high anisotropy ferromagnetic or ferrimagnetic particles is observed, with measurable values of both coercive field and remnant magnetization However, at higher temperatures, these features are washed out, especially at 310 K (normal human body temperature), a temperature for which no coercive field or remnant magnetization was observed [48].

To understand this behavior, additional magnetic moment measurements were carried out at low fields (2–20 mT) using the zero-field cooled (ZFC) and field-cooled (FC) methods (see Fig. 5 **a** and **b)**. There are three main points to note. First, both FC and ZFC curves show a steep decrease in magnetization for temperatures above 275 K,

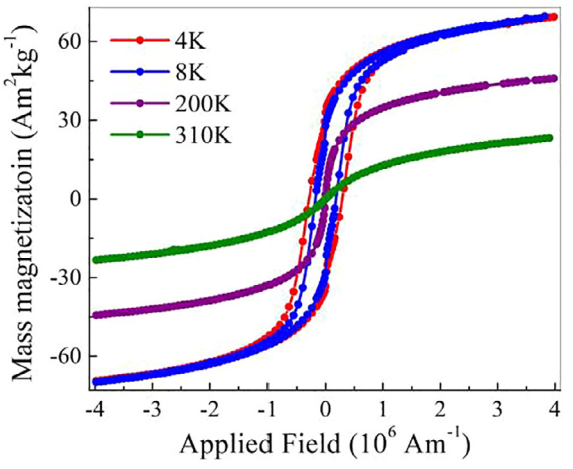

Fig. 4. Hysteresis loops of ferrite particles measured at different temperatures.

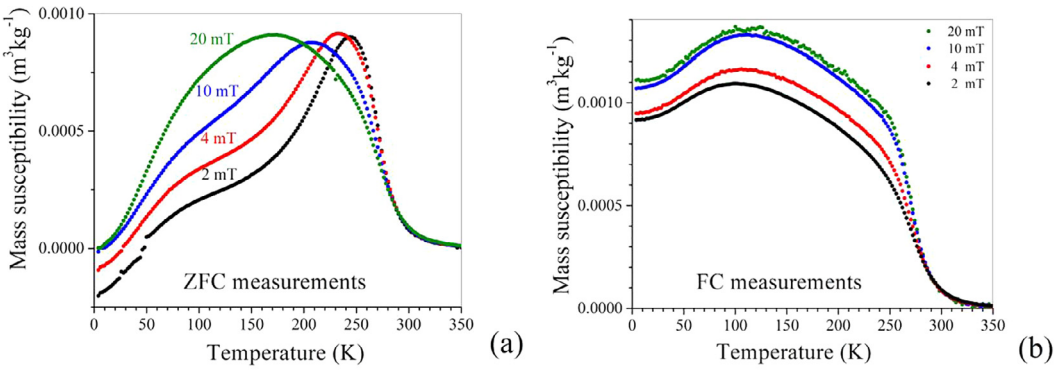

Fig. 5. Mass susceptibility as a function of temperature for applied fields from 2 mT to 20 mT. (a) zero-field cooled measurements (b) field-cooled measurements.

indicating that the Curie temperature for these nanoparticles is within this temperature region. This value of the Curie temperature is consistent with the broad range of values reported in the literature [42,49–52]. While ZFC curves typically display a peak and then a decrease in magnetization for increasing temperatures that follows a Langevin (1/T) dependence, the decrease observed in Fig. 5 is far steeper. The nanoparticles therefore are paramagnetic, rather than superparamagnetic, above 275 K.

Second, the mode blocking temperature is estimated to occur at lower temperatures than the ZFC peak, around T_B = 225 K. (It is important to note that many authors assume that the position of the ZFC peak corresponds to the mode blocking temperature, but this has recently been shown to be incorrect [53]. The mode blocking temperature, T_B, is defined as the temperature where particles at the peak of the size distribution become on average unblocked. For a log-normal distribution, the blocking temperature associated with the mode particle size occurs at lower temperature than the ZFC peak, due to small unblocked particles contributing disproportionately to the total magnetic moment of the sample). This blocking temperature corresponds to an estimated effective uniaxial anisotropy energy density $K = 25\ k_B\ T_B/V = 4\times10^4$ J/m^3, using the mode particle diameter of 16.5 nm. This value is 20% smaller than that reported in reference [54].

Third, there is an unusual peak in the FC curve for all field values used. This peak is reversible on heating and cooling, and shifts depending on the applied field used. Other authors reported a similar peak for zinc ferrite and cobalt zinc ferrite materials at roughly the same temperature [54–56]. Hochepied *et al.* [35] ruled out inter-particle dipolar interactions and field cooling rate effects, and instead attributed the peak to a reorientation of spins within the lattice as temperature is changed, which is possible in the presence of significant spin frustration [54]. While interesting from a fundamental perspective, the intended use of these materials at physiologically-relevant temperatures and under high applied field means this feature is not important for the thermometry application.

3.3. NMR measurements

We have measured longitudinal R_1 and transverse R_2 nuclear relaxivities (T_1 and T_2 relaxation rates) of protons in water using NMR at 3 T. Additionally, R_2^* was determined from the measured NMR linewidths $\nu_{1/2}$ (full width at half maximum) as $R_2^* = \pi\nu_{1/2}$ [40]. We note that each of these relaxations times can be used to create weighted MR images to achieve different contrasts. Below we discuss the different advantages of each measurement and the physics that each measurement describes. In our earlier work, we showed that micron-sized magnetic particles produce a temperature-dependent change in T_2^* [18], the transverse relaxation time associated with static perturbations in the magnetic field [57]. There is a disadvantage to this; the introduction of the magnetic nanoparticles and the resulting decrease in T_2^* leads to reduced brightness of the MR image, which is undesirable. In contrast to large particles, smaller nanoparticles have fluctuations in the orientation of the magnetization. This can influence the T_1 relaxation time, which is sensitive only to dynamic perturbations [58].

The ^{1}H NMR relaxivities were acquired at several temperatures between 278 and 323 K. The NMR temperature dependent R_2 relaxivity for pure agar and R_2 and R_2^* relaxivities for agar doped with nanoparticles (0.12 g/L) are shown in Fig. 6. The observed decrease in the R_2^* relaxivity as a function of temperature is consistent with the SQUID results of decreasing magnetization (see Fig. 3) and suggests that the nanoparticles could be used as temperature contrast agents for MR imaging. A strong correlation between measured temperature-dependent R_2^* relaxivity of water protons in the presence of ferrite particles and the temperature-dependent mass magnetization was confirmed by a high value of Pearson's correlation coefficient (0.9999). The decrease of the R_2^* value with increasing temperature is therefore directly related to the magnetic properties of the nanoparticles in strong magnetic field.

The R_2 relaxivity of protons in agar gel with nanoparticles is particularly interesting in that it increases slightly as temperature increases. It is known that R_2 and R_2^* are related through Eq. (1) [40,59]

$$R_2^* = R_2 + R_2^{'} = R_2 + \gamma\Delta B_0/2 + \gamma\Delta B_d/2 \quad (1)$$

where $R_2 = 1/T_2$, $R_2^{'}$ is the contribution from local magnetic field inhomogeneity, and γ is the gyromagnetic ratio for protons. In particular, $R_2^{'}$ has contributions from ΔB_0, that is the instrumental inhomogeneity originating from the nonuniformity of the constant applied field, B_o, used in NMR or MRI, and from, ΔB_d, which is the temperature dependent inhomogeneity from the magnetic nanoparticles.

Measuring both R_2 and R_2^* for pure agar and agar with embedded ferrite particles gives us an opportunity to extract the temperature-

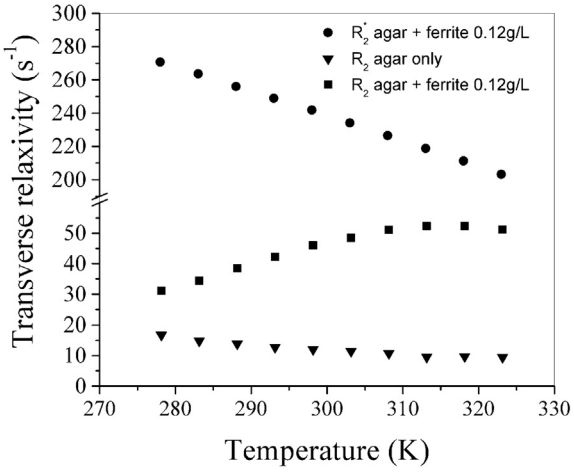

Fig. 6. Temperature dependence of transverse NMR relaxivities at an applied field of 3 T for particle concentration of 0.12 g/L and pure agar.

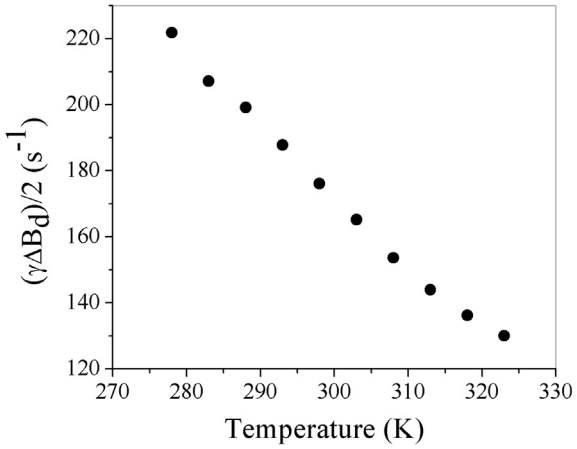

Fig. 7. Inhomogeneous water proton NMR line broadening from nanoparticles' dipolar field, $\gamma B_d/2$, as a function of temperature.

dependent contribution to the NMR linewidth from the particles' dipolar fields through Eq. (1). Results of $\gamma\Delta B_d/2$ in the temperature range of 275–325 K are presented in Fig. 7. Linear regression shows a clear linear dependence of $\gamma\Delta B_d/2$ as a function of temperature with Pearson's r = −0.997 and slope $-2.08\,s^{-1}K^{-1}$. Results are consistent with the temperature variation of the mass magnetization at the same 3 T magnetic field.

It is known that magnetic nanoparticles, including the standard iron-oxide nanoparticles, can create changes in R_1 [60]. Moreover, several iron oxide-based nanoparticles have already been developed with functionalized surfaces for specific applications [61,62]. In real clinical settings, after injection of nanoparticles, their exact spatial concentration in tissue is unknown.

However, information about concentration is necessary to accurately measure temperature, as discussed below in the next section. Simultaneous changes in R_1 and R_2 measurements may allow one to determine the spatial concentration of nanoparticles.

Firstly, nuclear spin-lattice relaxivity R_1 of water protons in agar gel (circles) and in agar gel with 0.12 g/L of ferrite nanoparticles (squares), as a function of temperature, are shown in Fig. 8. Pure agar gel exhibits a decrease of R_1 with temperature, similar to that reported in water [63,64]. The addition of nanoparticles increases the R_1 of the protons at higher temperature. One may expect that the increase in R_1 will scale with concentration, and this will be investigated in the future. This is important because ferrite nanoparticles under investigation have the potential to be a "positive" contrast material [65].

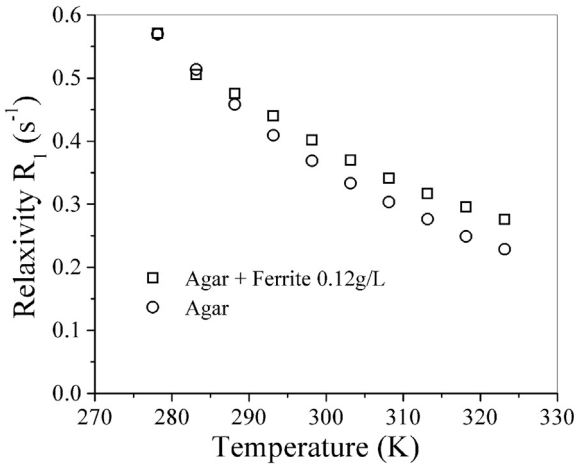

Fig. 8. Relaxivity R_1 of water protons in pure agar gel and agar gel with 0.12 g/L nanoparticle concentration at 3 T.

Secondly, an examination of R_2 and R_2^* data demonstrates that an introduction of nanoparticles causes a change in relaxivities. In particular, the R_2 data (Fig. 6) shows that with the ferrite particles added to the agar (squares) the R_2 value near body temperature is increased by over 5 times compared to the agar gel alone (triangles). One would expect the R_2 relaxivities to be strongly concentration dependent, providing another straightforward method to estimate nanoparticle concentration within each voxel of an MRI image. We note that combining T_1, T_2 and T_2^* weighted images was recently used to improve accuracy and sensitivity of *in vivo* brain structural analysis [66,67].

3.4. Stability

After one-year storage of particles in the dry form, their value of saturation magnetization dropped by 10%. For particles stored in an aqueous solution we noticed 8% drop in R_2^* relaxivity at 35 °C. This indicates that particles are stable, and their magnetization is only slightly changed over long periods of time. It is important to note that the observed changes in magnetic behavior following one year of storage are not expected to affect the ability of these particles to detect changes in temperature when employed within NMR line broadening and T_2^* contrast in gradient echo MR imaging schemes.

3.5. MRI measurements

A preclinical MRI scanner with a 30 cm 3 T superconductive horizontal magnet was used to determine how the brightness of MR images of the agar phantoms (described in the section above) varies as a function of both ferrite nanoparticle concentration and temperature.

An example series of images of two phantoms at different temperatures is provided in Fig. 9, showing both pure agar gel (top row) and agar gel with embedded particles with concentration of 0.12 g/L (bottom row). A gradually increasing image brightness as temperature increases can be seen for the gel containing particles (bottom row), whereas no change is seen for the pure agar gel (top row). Notice that these T_2^* weighted images are inherently darker, and their signal-to-noise ratio is lower than the corresponding proton density images would be [21,68]. To get the brightest images possible, we require the magnetization to drop fast with temperature but be as small as possible at the highest measured temperature.

A numerical comparison of relative MR image intensities as a function of temperature for two different particle concentrations is shown in Fig. 10. The relative intensity is defined as the ratio of the mean MR image brightness of the pure agar gel to the agar gel with ferrite particles embedded. The mean value and variance of individual image intensity was calculated using a program written in Matlab, after reconstruction of the image magnitude from the raw format of the scanner. Mean image intensity and corresponding variance was obtained from the area that covered the entire phantom axial cross-section of approximately 275 pixels. The standard deviation of image intensity ratios is calculated at each temperature and is displayed with error bars in Fig. 10. For both concentrations of particles, the relative image intensities display a nearly linear dependence as a function of temperature with slopes: -0.19 ± 0.01 and -0.48 ± 0.02 for particle concentrations of 0.12 g/L and 0.24 g/L, respectively. Although the value of the slope for the 0.24 g/L concentration is much higher than for the 0.12 g/L concentration, the substantial dimming of the image due to the presence of highly concentrated magnetic particles makes intensity measurements less accurate. Consequently, the error in brightness intensity propagates to the accuracy with which temperature can be determined by this method.

Using 95% confidence bands obtained from linear regression analysis, we estimate that at 310 K the temperature can be determined with accuracy of 1.0 K for 0.12 g/L and 1.75 K for 0.24 g/L concentration. Comparing with our previous report [18] using particles of 3.8 μm size and a concentration of 0.24 g/L (1.0 mM), we see that for 210 nm

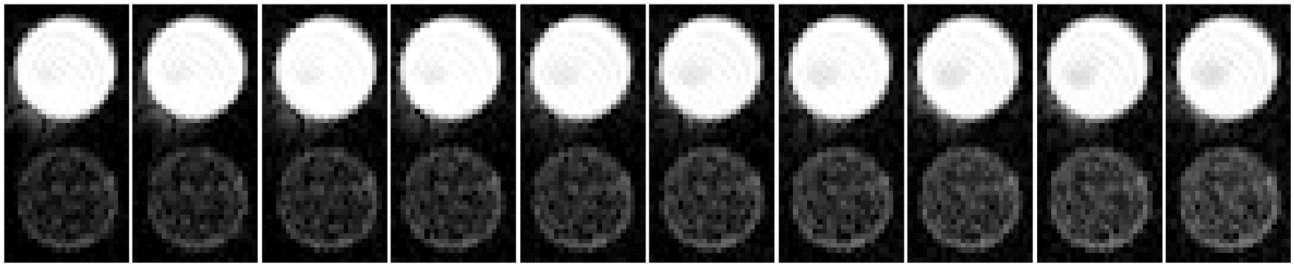

Fig. 9. Example of MRI image of the phantom with pure agar gel (top) and agar gel with embedded ferrite particles of 0.12 g/L concentration (bottom). As temperature increases, the images of the gel containing ferrite particles brighten due to the reduction of magnetic dipolar field originating from particles.

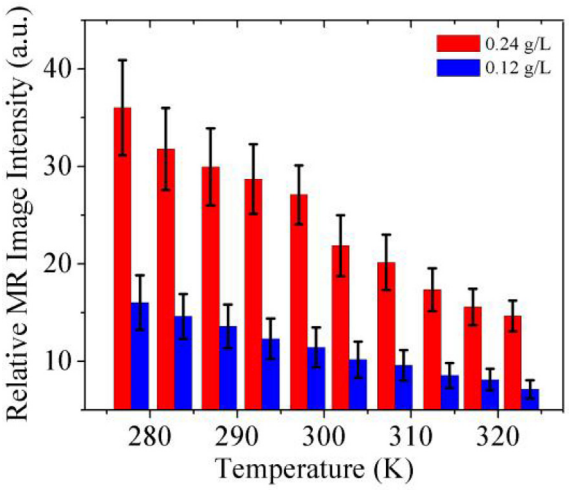

Fig. 10. The ratio of mean MR image brightness of pure agar gel to agar gel with embedded ferrite particles as a function of temperature in a field of 3 T, for two different concentrations; 0.12 g/L (blue bars) and 0.24 g/L (red bars). The error bars display the calculated standard deviations of image intensity ratios (relative to the pure agar image) at each temperature. Note higher errors for 0.24 g/L concentration as signal-to-noise decreases in MR images with higher nanoparticles concentration. (For interpretation of the references to colour in this figure legend, the reader is referred to the web version of this article.)

agglomerates of particles, the thermal accuracy is slightly worse, namely 1.75 K versus 1.3 K. Even though the slope value is larger (-0.48 ± 0.02 versus $-0.36 \pm 0.03\,K^{-1}$), the accuracy is worse due to darker images. This observation confirms our theoretical prediction that similar concentrations of much smaller particles can produce comparable thermal effects on MR image brightness [18].

4. Conclusions

This study presents the first-use of 210 nm ferrite nanoparticle agglomerates as MRI temperature sensors. We found that a temperature resolution of 1.0 K is possible across the range of medically relevant physiological temperatures. As we have shown, data on all the water protons' nuclear relaxivities should provide information on particle density and temperature in each voxel. This is particularly important in clinical applications where the density of nanoparticles in the treated tissue is not likely to be uniform or known initially. Furthermore, many MRI-guided interventional procedures, such as thermal ablation, require a determination of temperature with a precision of only 3–5 K [69]. Our method thus seems to be appropriate for such applications [70].

Making contrast agents consisting of 210 nm-diameter agglomerates of particles is an intermediate step between the micrometer size particles that were made previously [20] and 50 nm particles, which are needed for intravenous delivery. This is important step in order to understand the thermal response of particles and their influence on MR images as particle size becomes smaller and smaller. Note that the thermal diffusion of protons across regions containing smaller particles may change the R_2^* weighted MR images [71–74]. Also, even though these particles are currently too big for intravenous delivery, we envision use of such particles embedded in silicone rubber patches, or similar devices, that can be used in cranial MRI guided focused ultrasound ablations to monitor external skull temperature.

5. Declaration of interest

None.

Acknowledgements

This project was made possible with support from an I-Corps NSF Grant to ZC and JHH #17-013. We thank Drs. T.K. Yasar and T.J. Royston from University of Illinois at Chicago for making the Matlab program available for image intensity calculations. JHH thanks Kristen Petersen and Tim S. Read for their help editing the manuscript, Dr. Yuriy Garbovskiy for conducting DLS study, and Joshua Richman from Cornell University for his assistance with the NMR samples and MRI phantom preparation.

References

[1] V. Rieke, K. Butts Pauly, MR thermometry, J. Magn. Reson. Imaging 27 (2008) 376–390, https://doi.org/10.1002/jmri.21265.
[2] L. Winter, E. Oberacker, K. Paul, Y. Ji, C. Oezerdem, P. Ghadjar, A. Thieme, V. Budach, P. Wust, T. Niendorf, Magnetic resonance thermometry: methodology, pitfalls and practical solutions, Int. J. Hyperthermia 32 (2016) 63–75, https://doi.org/10.3109/02656736.2015.1108462.
[3] E.M. Kardoulaki, R.R.A. Syms, I.R. Young, MRI for noninvasive thermometry, in: R.K. Harris, R.L. Wasylishe (Eds.), EMagRes, John Wiley & Sons, Ltd, Chichester, UK, 2016, pp. 1203–1218, , https://doi.org/10.1002/9780470034590.emrstm1103.
[4] S.S. Evans, E.A. Repasky, D.T. Fisher, Fever and the thermal regulation of immunity: the immune system feels the heat, Nat. Rev. Immunol. 15 (2015) 335–349, https://doi.org/10.1038/nri3843.
[5] M. Bakkers, C.G. Faber, J.P.H. Reulen, J.G.J. Hoeijmakers, E.K. Vanhoutte, I.S.J. Merkies, Optimizing temperature threshold testing in small-fiber neuropathy: temperature testing protocol, Muscle Nerve 51 (2015) 870–876, https://doi.org/10.1002/mus.24473.
[6] J. Saito, S. Noguchi, E. Hashiba, F. Kimura, T. Kushikata, I. Fukuda, K. Hirota, Usefulness of temperature gradient during cardiopulmonary bypass for diagnosis of misplacement of a frozen elephant trunk, J. Cardiothorac. Vasc. Anesth. 31 (2017) 266–269, https://doi.org/10.1053/j.jvca.2016.05.010.
[7] D.A. Kennedy, T. Lee, D. Seely, A comparative review of thermography as a breast cancer screening technique, Integr. Cancer Ther. 8 (2009) 9–16, https://doi.org/10.1177/1534735408326171.
[8] D.A. Woodrum, A. Kawashima, K.R. Gorny, L.A. Mynderse, Prostate cancer: state of the art imaging and focal treatment, Clin. Radiol. 72 (2017) 665–679, https://doi.org/10.1016/j.crad.2017.02.010.
[9] K. Kuroda, MR techniques for guiding high-intensity focused ultrasound (HIFU) treatments, J. Magn. Reson. Imaging 47 (2017) 316–331, https://doi.org/10.1002/jmri.25770.
[10] M. Zhu, Z. Sun, C.K. Ng, Image-guided thermal ablation with MR-based thermometry, Quant. Imaging Med. Surg. 7 (2017) 356–368, https://doi.org/10.21037/qims.2017.06.06.
[11] J. de Poorter, C. de Wagter, Y. de Deene, C. Thomsen, F. Stahlberg, E. Achten, The proton-resonance-frequency-shift method compared with molecular diffusion for quantitative measurements of two-dimensional time dependent temperature

distribution in a phantom, J. Magn. Reson. 103 (1994) 234–241, https://doi.org/10.1006/jmrb.1994.1035.
[12] K.K. Vigen, B.L. Daniel, J.M. Pauly, K. Butts., Triggered, navigated, multi- baseline method for proton resonance frequency temperature mapping with respiratory motion, Magn. Reson. Med. 50 (2003) 1003–1010, https://doi.org/10.1002/mrm.10608.
[13] J. de Poorter, C. de Wagter, Y. de Deene, C. Thomsen, F. Stahlberg, F.E. Achten, Noninvasive MRI thermometry with the proton resonance frequency (PRF) method: in vivo results in human muscle, Magn. Reson. Med. 33 (1995) 74–81, https://doi.org/10.1002/mrm.1910330111.
[14] A. Boss, H. Graf, B. Muller-Bierl, S. Clasen, D. Schmidt, P.L. Pereira, F. Schick, Magnetic susceptibility effects on the accuracy of MR temperature monitoring by the proton resonance frequency method, J. Magn. Reson. Imaging 22 (2005) 813–820, https://doi.org/10.1002/jmri.20438.
[15] K. Kuroda, K. Oshio, A.H. Chung, K. Hynynen, F.A. Jolesz, Temperature mapping using the water proton chemical shift: a chemical shift selective phase mapping method, Magn. Reson. Med. 38 (1997) 845–851, https://doi.org/10.1002/mrm.1910380523.
[16] J.A. de Zwart, P. van Gelderen, D.J. Kelly, C.T. Moonen, Fast magnetic-resonance temperature imaging, J. Magn. Reson. B 112 (1996) 86–90, https://doi.org/10.1006/jmrb.1996.0115.
[17] J. Yuan, C.S. Mei, L.P. Panych, N.J. McDannold, B. Madore, Towards fast and accurate temperature mapping with proton resonance frequency-based MR thermometry, Quant. Imaging Med. Surg. 2 (2012) 21–32, https://doi.org/10.3978/j.issn.2223-4292.2012.01.06.
[18] J.H. Hankiewicz, Z. Celinski, K.F. Stupic, N.R. Anderson, R.E. Camley, Ferromagnetic particles as magnetic resonance imaging temperature sensors, Nat. Commun. 27 (2016) 12415, https://doi.org/10.1038/ncomms12415.
[19] J.H. Hankiewicz, N. Alghamdi, N.M. Hammelev, N.R. Anderson, R.E. Camley, K. Stupic, M. Przybylski, J. Zukrowski, Z.J. Celinski, Zinc doped copper ferrite particles as temperature sensors for magnetic resonance imaging, AIP Adv. 7 (2017) 056703, , https://doi.org/10.1063/1.4973439.
[20] N.A. Alghamdi, J.H. Hankiewicz, N.R. Anderson, K.F. Stupic, R.E. Camley, M. Przybylski, J. Zukrowski, Z. Celinski, Development of ferrite-based temperature sensors for magnetic resonance imaging: study of Cu1-xZnxFe2O4, Phys. Rev. Appl. 9 (2018) 054030–054040, https://doi.org/10.1103/PhysRevApplied.9.054030.
[21] G.B. Chavhan, P.S. Babyn, B. Thomas, M.M. Shroff, E.M. Haacke, Principles, techniques, and applications of T_2^*-based MR imaging and its special applications, RadioGraphics 29 (2009) 1433–1449, https://doi.org/10.1148/rg.295095034.
[22] P. Kokeny, Y.-C.N. Cheng, H. Xie, A study of MRI gradient echo signals from discrete magnetic particles with considerations of several parameters in simulations, Magn. Reson. Imaging 48 (2018) 129–137, https://doi.org/10.1016/j.mri.2017.12.019.
[23] V. Kononenko, M. Narat, D. Drobne, Nanoparticle interaction with the immune system/Interakcije nanodelcev z imunskim sistemom, Arch. Ind. Hyg. Toxicol. 66 (2015) 97–108, https://doi.org/10.1515/aiht-2015-66-2582.
[24] N. Lee, T. Hyeon, Designed synthesis of uniformly sized iron oxide nanoparticles for efficient magnetic resonance imaging contrast agents, Chem. Soc. Rev. 41 (2012) 2575–2589, https://doi.org/10.1039/C1CS15248C.
[25] S. Ramachandran, A review on ferrite devices, IETE J. Res. 9 (1963) 600–623, https://doi.org/10.1080/03772063.1963.11486506.
[26] H. Shokrollahi, A. Khorramdin, Gh. Isapour., Magnetic resonance imaging by using nano-magnetic particles, J. Magn. Magn. Mater. 369 (2014) 176–183, https://doi.org/10.1016/j.jmmm.2014.06.023.
[27] N. Daffé, F. Choueikani, S. Neveu, M.-A. Arrio, A. Juhin, P. Ohresser, V. Dupuis, P. Sainctavit, Magnetic anisotropies and cationic distribution in $CoFe_2O_4$ nanoparticles prepared by co-precipitation route: influence of particle size and stoichiometry, J. Magn. Magn. Mater. 460 (2018) 243–252, https://doi.org/10.1016/j.jmmm.2018.03.041.
[28] R. Valenzuela, Novel applications of ferrites, Phys. Res. Inter. 2012 (2012) 1–9, https://doi.org/10.1155/2012/591839.
[29] M. Taupitz, S. Schmitz, B. Hamm, Superparamagnetische Eisenoxidpartikel: Aktueller Stand und zukünftige Entwicklungen, Fortschr. Röntgenstr. 175 (2003) 752–765, https://doi.org/10.1055/s-2003-39935.
[30] A. Ba-Ssalamah, M. Uffmann, S. Saini, N. Bastati, C. Herold, W. Schima, Clinical value of MRI liver-specific contrast agents: a tailored examination for a confident non-invasive diagnosis of focal liver lesions, Eur. Radiol. 19 (2009) 342–357, https://doi.org/10.1007/s00330-008-1172-x.
[31] F. Ahmad, Y. Zhou, Pitfalls and challenges in nanotoxicology: a case of cobalt ferrite ($CoFe_2O_4$) nanocomposites, Chem. Res. Toxicol. 30 (2017) 492–507, https://doi.org/10.1021/acs.chemrestox.6b00377.
[32] S. Matsuda, T. Nakanishi, K. Kaneko, T. Osaka, Synthesis of cobalt ferrite nanoparticles using spermine and their effect on death in human breast cancer cells under an alternating magnetic field, Electrochim. Acta 183 (2015) 153–159, https://doi.org/10.1016/j.electacta.2015.06.108.
[33] J. Lu, S. Ma, J. Sun, C. Xia, C. Liu, Z. Wang, X. Zhao, F. Gao, Q. Gong, B. Song, Manganese ferrite nanoparticle micellar nanocomposites as MRI contrast agent for liver imaging, Biomaterials 30 (2009) 2919–2928, https://doi.org/10.1016/j.biomaterials.2009.02.001.
[34] Z. Hedayatnasab, F. Abnisa, W.M.A.W. Daud, Review on magnetic nanoparticles for magnetic nanofluid hyperthermia application, Mater. Des. 123 (2017) 174–196, https://doi.org/10.1016/j.matdes.2017.03.036.
[35] S. Li, V.T. John, C. O'Connor, V. Harris, E. Carpenter, Cobalt-ferrite nanoparticles: structure, cation distributions, and magnetic properties, J. Appl. Phys. 87 (2000) 6223–6225, https://doi.org/10.1063/1.372661.
[36] S. Ayyappan, S. Mahadevan, P. Chandramohan, M.P. Srinivasan, J. Philip, B. Raj, Influence of Co^{2+} ion concentration on the size, magnetic properties, and purity of $CoFe_2O_4$ spinel ferrite nanoparticles, J. Phys. Chem. C 114 (2010) 6334–6341, https://doi.org/10.1021/jp911966p.
[37] T. Fujita, B. Jeyadevan, M. Mamiya, Preparation of temperature sensitive magnetic fluid, J. Soc. Mater. Eng. Resour. Jpn. 3 (1990) 43–48, https://doi.org/10.5188/jsmerj.3.43.
[38] H. Iida, K. Takayanagi, T. Nakanishi, T. Osaka, Synthesis of Fe_3O_4 nanoparticles with various sizes and magnetic properties by controlled hydrolysis, J. Colloid Interface Sci. 314 (2007) 274–280, https://doi.org/10.1016/j.jcis.2007.05.047.
[39] T. Osaka, T. Nakanishi, S. Shanmugam, S. Takahama, H. Zhang, Effect of surface charge of magnetite nanoparticles on their internalization into breast cancer and umbilical vein endothelial cells, Colloids Surf., B Biointerfaces 71 (2009) 325–330, https://doi.org/10.1016/j.colsurfb.2009.03.004.
[40] T.C. Farrar, E.D. Becker, Pulse and Fourier Transform NMR; Introduction to Theory and Methods, Academic Press, New York, 1971.
[41] M.A. Bernstein, K.F. King, Z/J. Zhou, Handbook of MRI Pulse Sequences, Academic Press, Amsterdam; Boston, 2004.
[42] I. Sharifi, H. Shokrollahi, Nanostructural, magnetic and Mössbauer studies of nanosized $Co_{1-x}Zn_xFe_2O_4$ synthesized by co-precipitation, J. Magn. Magn. Mater. 324 (2012) 2397–2403, https://doi.org/10.1016/j.jmmm.2012.03.008.
[43] A.L. Patterson, The Scherrer formula for X-Ray particle size determination, Phys. Rev. 56 (1939) 978–982, https://doi.org/10.1103/PhysRev. 56.978.
[44] Z. Zhou, R. Tian, Z. Wang, Z. Yang, Y. Liu, G. Liu, R. Wang, J. Gao, J. Song, L. Nie, X. Chen, Artificial local magnetic field inhomogeneity enhances T_2 relaxivity, Nat. Commun. 8 (2017), https://doi.org/10.1038/ncomms15468.
[45] M. Veverka, Z. Jirák, O. Kaman, K. Knizek, M. Marysko, E. Pollert, K. Zaveta, A. Lancok, M. Dlouha, S. Vratisvlav, Distribution of cations in nanosize and bulk Co–Zn ferrites, Nanotechnology 22 (2011) 345701, , https://doi.org/10.1088/0957-4484/22/34/345701.
[46] M.B. Ali, K. El Maalam, H. El Moussaoui, O. Mounkachi, O. Hamedoun, R. Masrour, E.K. Hlil, A. Benyoussef, Effect of zinc concentration on the structural and magnetic properties of mixed Co-Zn ferrites nanoparticles synthesized by Sol/Gel method, J. Magn. Magn. Mater. 398 (2015) 20–25, https://doi.org/10.1016/j.jmmm.2015.08.097.
[47] H. Parmar, P. Acharya, R.V. Upadhyay, V. Siruguri, S. Rayaprol, Low temperature magnetic ground state in bulk Co0.3Zn0.7Fe2O4 spinel ferrite system: neutron diffraction, magnetization and ac-susceptibility studies. 153 (2013) 60–65. 10.1016/j.ssc.2012.09.021.
[48] M.D. Glinchuk, A.V. Ragulya, V.A. Stephanovich, The peculiar physical properties of nanosized ferroics, Nanoferroics 177 (2013) 33–89, https://doi.org/10.1007/978-94-007-5992-3_2.
[49] S. Nasrin, Influence of Zn substitution on the structural and magnetic properties of $Co_{1-x}Zn_xFe_2O_4$ nano-ferrites, IOSR J. Appl. Phys. 6 (2014) 58–65, https://doi.org/10.9790/4861-06235865.
[50] C. Gomez-Polo, S. Larumbe, J. Beato-Lopez, E. Mendonca, C. De Meneses, J. Duque, Self-regulated magnetic induction heating of Zn-Co ferrite nanoparticles, IEEE International Magnetics Conference (INTERMAG), 2015, https://doi.org/10.1109/INTMAG.2015.7157443 Beijing China.
[51] I.H. Gul, A.Z. Abbasi, F. Amin, M. Anis-ur-Rehman, A. Maqsood, Structural, magnetic and electrical properties of $Co_{1-x}Zn_xFe_2O_4$ synthesized by co-precipitation method, J. Magn. Magn. Mater 311 (2007) 494–499, https://doi.org/10.1016/j.jmmm.2006.08.005.
[52] S.S. Jadhav, S.E. Shirsath, S.M. Patange, K.M. Jadhav, Effect of Zn substitution on magnetic properties of nanocrystalline cobalt ferrite, J. Appl. Phys. 108 (2010) 093920, , https://doi.org/10.1063/1.3499346.
[53] I.J. Bruvera, P. Mendoza Zélis, M. Pilar Calatayud, G.F. Goya, F.H. Sánchez, Determination of the blocking temperature of magnetic nanoparticles: the good, the bad, and the ugly, J. Appl. Phys. 118 (2015) 184304, https://doi.org/10.1063/1.4935484.
[54] J.F. Hochepied, P. Bonville, M.P. Pileni, Nonstoichiometric zinc ferrite nanocrystals: syntheses and unusual magnetic properties, J. Phys. Chem. B 104 (2000) 905–912, https://doi.org/10.1021/jp991626i.
[55] S. Ammar, N. Jouini, F. Fiévet, Z. Beji, L. Smiri, P. Moline, M. Danot, J.M. Greneche, Magnetic properties of zinc ferrite nanoparticles synthesized by hydrolysis in a polyol medium, J. Phys. Condens. Matter. 18 (2006) 9055–9069, https://doi.org/10.1088/0953-8984/18/39/032.
[56] J.F. Hochepied, M.P. Pileni, Magnetic properties of mixed cobalt–zinc ferrite nanoparticles, J. Appl. Phys. 86 (2000) 2472–2478, https://doi.org/10.1063/1.372205.
[57] R.N. Muller, P. Gillis, F. Moiny, A. Roch, Transverse relaxivity of particulate MRI contrast media: from theories to experiments, Magn. Reson. Med. 22 (1991) 178–182, https://doi.org/10.1002/mrm.1910220203.
[58] H. Rorschach, A classical theory of NMR relaxation processes, J. Magn. Reson. 1967 (67) (1986) 519–530, https://doi.org/10.1016/0022-2364(86)90388-4.
[59] E.M. Haacke, N.Y.C. Cheng, M.J. House, Q. Liu, J. Neelavalli, R.J. Ogg, A. Khan, M. Ayaz, W. Kirsch, A. Obenaus, Imaging iron stores in the brain using magnetic resonance imaging, Magn. Reson. Imaging 23 (2005) 1–25, https://doi.org/10.1016/j.mri.2004.10.001.
[60] C.G. Hadjipanayis, M.J. Bonder, S. Balakrishnan, X. Wang, H. Mao, G.C. Hadjipanayis, Metallic iron nanoparticles for MRI contrast enhancement and local hyperthermia, Small 4 (2008) 1925–1929, https://doi.org/10.1002/smll.200800261.
[61] J.H. Lee, Y.M. Huh, Y.W. Jun, J.W. Seo, J.T. Jang, H.T. Song, S. Kim, E.J. Cho, H.G. Yoon, J.S. Suh, J. Cheon, Artificially engineered magnetic nanoparticles for ultra-sensitive molecular imaging, Nat. Med. 13 (2007) 95–99, https://doi.org/10.1038/nm1467.
[62] R.S. Chaughule, S. Purushotham, R.V. Ramanujan, Magnetic nanoparticles as

contrast agents for magnetic resonance imaging, Proc. Natl. Acad. Sci. India Sect. Phys. Sci. 82 (2012) 257–268, https://doi.org/10.1007/s40010-012-0038-4.
[63] J.C. Hindman, A. Svirmickas, M. Wood, Relaxation processes in water. A study of the proton spin-lattice relaxation time, J. Chem. Phys. 59 (1973) 1517–1522, https://doi.org/10.1063/1.1680209.
[64] K. Krynicki, Proton spin-lattice relaxation in pure water between 0 °C and 100 °C, Physica 32 (1966) 167–178, https://doi.org/10.1016/0031-8914(66)90113-3.
[65] H. Wei, O.T. Bruns, M.G. Kaul, E.C. Hansen, M. Barch, A. Wiśniowska, O. Chen, Y. Chen, N. Li, S. Okada, J.M. Cordero, M. Heine, C.T. Farrar, D.M. Montana, G. Adam, H. Ittrich, A. Jasanoff, P. Nielsen, M.G. Bawendi, Exceedingly small iron oxide nanoparticles as positive MRI contrast agents, Proc. Natl. Acad. Sci. 114 (2017) 2325–2330, https://doi.org/10.1073/pnas.1620145114.
[66] M. Misaki, J. Savitz, V. Zotev, R. Phillips, H. Yuan, K.D. Young, W.C. Drevets, J. Bodurka, Contrast enhancement by combining T1- and T2-weighted structural brain MR Images: contrast enhancement with T_{1w} and T_{2w} MRI, Magn. Reson. Med. 74 (2015) 1609–1620, https://doi.org/10.1002/mrm.25560.
[67] C. Bazelaire, N.M. Rofsky, G. Duhamel, J. Zhang, M.D. Michaelson, D. George, D.C. Alsop, Combined T_2* and T_1 measurements for improved perfusion and permeability studies in high field using dynamic contrast enhancement, Eur. Radiol. 16 (2006) 2083–2091, https://doi.org/10.1007/s00330-006-0198-1.
[68] R. Bitar, G. Leung, R. Perng, S. Tadros, A.R. Moody, J. Sarrazin, C. McGregor, M. Christakis, S. Symons, A. Nelson, T.P. Roberts, MR pulse sequences: what every radiologist wants to know but is afraid to ask, RadioGraphics 26 (2006) 513–537, https://doi.org/10.1148/rg.262055063.
[69] D.A. Woodrum. Private Communication. January 2018.
[70] A. Copelan, J. Hartman, M. Chehab, A. Venkatesan, High-intensity focused ultrasound: current status for image-guided therapy, Semin. Interv. Radiol. 32 (2015) 398–415, https://doi.org/10.1055/s-0035-1564793.
[71] D.A. Yablonskiy, E.M. Haacke, Theory of NMR signal behavior in inhomogeneous tissues: the static dephasing regime, Magn. Reson. Med. 32 (1994) 749–763, https://doi.org/10.1002/mrm.1910320610.
[72] C. Chouly, D. Pouliquen, I. Lucet, J.J. Jeune, P. Jallet, Development of superparamagnetic nanoparticles for MRI: effect of particle size, charge and surface nature on biodistribution, J. Microencapsul. 13 (1996) 245–255, https://doi.org/10.3109/02652049609026013.
[73] G. Huang, H. Li, J. Chen, Z. Zhao, L. Yang, X. Chi, Z. Chen, X. Wang, J. Gao, Tunable T_1 and T_2 contrast abilities of manganese-engineered iron oxide nanoparticles through size control, Nanoscale 6 (2014) 10404–10412, https://doi.org/10.1039/C4NR02680B.
[74] E.M. Haacke, S. Liu, S. Buch, W. Zheng, D. Wu, Y. Ye, Quantitative susceptibility mapping: current status and future directions, Magn. Reson. Imaging 33 (2015) 1–25, https://doi.org/10.1016/j.mri.2014.09.004.